PNAS RESEARCH ARTICLE | BIOCHEMISTRY

Mechanistic analysis of a novel membrane-interacting variable loop in the pleckstrin-homology domain critical for dynamin function

Himani Khurana[a], Krishnakanth Baratam[b], Soumya Bhattacharyya[a], Anand Srivastava[b], and Thomas J. Pucadyil[a,1]

Edited by James Hurley, University of California Berkeley, Berkeley, CA; received September 6, 2022; accepted February 8, 2023

Classical dynamins are best understood for their ability to generate vesicles by membrane fission. During clathrin-mediated endocytosis (CME), dynamin is recruited to the membrane through multivalent protein and lipid interactions between its proline-rich domain (PRD) with SRC Homology 3 (SH3) domains in endocytic proteins and its pleckstrin-homology domain (PHD) with membrane lipids. Variable loops (VL) in the PHD bind lipids and partially insert into the membrane thereby anchoring the PHD to the membrane. Recent molecular dynamics (MD) simulations reveal a novel VL4 that interacts with the membrane. Importantly, a missense mutation that reduces VL4 hydrophobicity is linked to an autosomal dominant form of Charcot-Marie-Tooth (CMT) neuropathy. We analyzed the orientation and function of the VL4 to mechanistically link data from simulations with the CMT neuropathy. Structural modeling of PHDs in the cryo-electron microscopy (cryo-EM) cryoEM map of the membrane-bound dynamin polymer confirms VL4 as a membrane-interacting loop. In assays that rely solely on lipid-based membrane recruitment, VL4 mutants with reduced hydrophobicity showed an acute membrane curvature-dependent binding and a catalytic defect in fission. Remarkably, in assays that mimic a physiological multivalent lipid- and protein-based recruitment, VL4 mutants were completely defective in fission across a range of membrane curvatures. Importantly, expression of these mutants in cells inhibited CME, consistent with the autosomal dominant phenotype associated with the CMT neuropathy. Together, our results emphasize the significance of finely tuned lipid and protein interactions for efficient dynamin function.

structural modeling | biochemical reconstitution | nanotubes | membrane insertion and fission | BIN1 scaffolds

Significance

During clathrin-mediated endocytosis (CME), endocytic proteins recruit dynamin which self-assembles around the necks of coated buds and generates vesicles through membrane fission. Dynamin engages with the membrane using its pleckstrin-homology domain (PHD). Recent molecular dynamics simulations reveal a novel membrane-inserting loop in the PHD, and a missense mutation that reduces loop hydrophobicity is linked to an autosomal dominant form of Charcot-Marie-Tooth (CMT) neuropathy. Here, we report that a mild reduction in loop hydrophobicity causes severe defects in dynamin-catalyzed fission. Our results emphasize how small perturbations to protein–lipid interactions can have a significant impact on dynamin functions.

Dynamins contain a G domain, a stalk domain, and a bundle-signaling element (BSE). The G domain hydrolyzes guanosine triphosphate (GTP), and the stalk maintains dynamin as a tetramer in solution. The stalk also facilitates self-assembly into helical scaffolds on the membrane. The BSE transmits self-assembly induced conformational changes in the scaffold to the G domain causing stimulation in dynamin's basal GTPase activity (1–3). In addition to these core domains, classical dynamins contain an additional membrane binding pleckstrin-homology domain (PHD) and a proline-rich domain (PRD). The PHD binds phosphatidylinositol-4,5-bisphosphate [$PI(4,5)P_2$] and phosphatidylserine (PS), while the PRD binds SRC Homology 3 (SH3) domains in endocytic accessory proteins. Multivalent binding to endocytic proteins and lipids serves to recruit dynamin to emergent membrane buds during clathrin-mediated endocytosis (CME) (4–8).

The PHD contains a core β-sandwich that is formed of two sheets oriented in an antiparallel arrangement and a single α-helix (9, 10). The β strands are connected by variable loops (VLs). VL1 (^{531}IGIMKGG) is a membrane-inserting loop and mutations that reduce its hydrophobicity render dynamin defective in membrane binding, fission, and CME (11–13). Recent molecular dynamics (MD) simulations of the isolated PHD on a planar membrane confirm membrane insertion of the VL1, with the terminal atom on the I533 residue at the tip of VL1 dipping 0.58 nm below the phosphate plane (14). The relatively polar VL2 (^{554}KDDEEKE) and VL3 (^{590}NTEQRNVYKDY) are important for dynamin functions (15, 16). They however do not directly partition into but remain proximal to the membrane with limited interactions with negative-charged lipids (14). The PHD structure shows a fourth VL (VL4) (^{576}EKGFMSSK) located between β5 and β6 strands, and MD simulations show that it interacts directly with the membrane (14). This is surprising considering that VL4 has much lower hydrophobicity than VL1. VL4 could therefore represent a novel membrane-interacting loop which together with VL1 anchors the PHD on to the membrane. The PHD is a hotspot for mutations linked to several genetic disorders. Mutations

Author affiliations: [a]Indian Institute of Science Education and Research, Pune 411008, India; and [b]Molecular Biophysics Unit, Indian Institute of Science, Bengaluru 560012, India

Author contributions: H.K., K.B., S.B., A.S., and T.J.P. designed research; H.K. and S.B. performed research; H.K., K.B., and S.B. contributed new reagents/analytic tools; H.K., K.B., S.B., and T.J.P. analyzed data; and H.K., K.B., A.S., and T.J.P. wrote the paper.

The authors declare no competing interest.

This article is a PNAS Direct Submission.

[1]To whom correspondence may be addressed. Email: pucadyil@iiserpune.ac.in.

This article contains supporting information online at https://www.pnas.org/lookup/suppl/doi:10.1073/pnas.2215250120/-/DCSupplemental.

Published March 8, 2023.

causing centronuclear myopathy (CNM) and Charcot-Marie-Tooth (CMT) neuropathy are predominantly located in this domain (17–22). CNM mutations map to a region on the PHD distant from those required for lipid binding, while CMT mutations are frequently localized in the PHD and affect lipid binding (22). Importantly, a missense mutation M580T in VL4 has been linked to an autosomal dominant form of CMT (18). MD simulations reveal that the adjacent F579 residue in VL4 approaches closest to the membrane, with the terminal atom dipping 0.41 nm below the phosphate plane (14). Surprisingly, simulations with the F579A mutant showed no apparent defect in membrane binding. Instead, this mutant, missing one of the two membrane-interacting pivots, rendered the PHD to sample a wider range of orientations about the membrane normal.

To mechanistically link data from MD simulations to the CMT neuropathy, we analyzed functions of the VL4 using structural modeling and reconstitution assays that monitor dynamin functions.

Results

Structural Modeling of the PHD in the Membrane-Bound Dynamin Polymer Indicates that VLs Are Proximal to the Membrane. The VLs show a high degree of conservation across dynamin isoforms and across dynamins from different species (*SI Appendix*, Fig. S1). To test predictions from simulations that VL4 is a membrane-interacting loop, we modeled the PHD into the 3.75 Å resolution cryo-EM map of the membrane-bound Dyn1ΔPRD polymer (23) (*SI Appendix*, Fig. S2). We then extracted radial distances of cα atoms in the 518 to 630 residue long PHD from the axis of assembly in the 46 dynamin molecules in the polymer (*SI Appendix*, Fig. S2). The low resolution of the cryo-EM map disallowed accurate demarcation of the membrane surface. We therefore plotted distances on a relative scale, with the distance of the residue closest to the axis of assembly defined as zero (Fig. 1*A*, gray). The cα atom distances revealed from previous MD simulations of the PHD on a planar membrane are also shown for comparison (Fig. 1*A*, magenta) (14). A cursory look at the profiles reveals good correspondence between the cα atom distances from modeling and simulations around the VL1 (531 to 537) and VL4 (576 to 583) residues, but not so much around the VL2 (554 to 560) and VL3 (590 to 600) residues. To better understand this data, we parsed the 46 profiles into clusters based on the VL that approaches closest to the axis of assembly (and therefore the membrane). Fig. 1*B* shows this data as a heat map, with red marking residues close to the membrane and blue marking residues distant from the membrane. Such analysis reveals that 17 of the 46 PHDs have the VL1 approaching closest to the membrane, making it the most abundant cluster. Importantly, 13 of the 46 PHDs have the VL4 approaching closest to the membrane and were followed by VL3 (11 of 46) and VL2 (4 of 46). One of the 46 PHDs showed an anomalous distribution of residue distances. Based on proximity to the membrane, VLs therefore display an order of 1>4>3≫2 in abundance in the membrane-bound dynamin polymer. A significant number of PHDs have the VL3 oriented close to the membrane, which was not the case with simulations of the PHD on a planar membrane where the VL3 only maintained proximity to the headgroups of negatively charged lipids (14). Since the cryo-EM map reflects orientation of the PHD on a curved membrane tube, this difference emphasizes the function of VL3 in membrane curvature induction and stabilization, consistent with previous studies (16). Furthermore, individual VLs in the PHD appear to orient themselves in a somewhat exclusive manner. Thus, in the VL1 cluster, a significant fraction of VL4 orients away from the membrane. This is also the case for VL1 in the VL3 cluster and for VL2 in the VL4 cluster.

Reducing VL4 Hydrophobicity Causes Dynamin Functions to Become Sensitive to Membrane Curvature. We tested the importance of VL4 to dynamin function by mutating the tip residue F579 to alanine, which would reduce loop hydrophobicity. The PHD contains positively charged clusters towards the membrane binding interface (*SI Appendix*, Fig. S3*A*). MD simulations reveal that lysine residues outside the VLs (K539 and K554) and within VL1 (K535) recruit the anionic lipid 1,2-dioleoyl-sn-glycero-3-phospho-L-serine (sodium salt) (DOPS) toward the PHD and stabilize its membrane association (14). To rule out potential global defects caused by introducing the F579A mutation and establish the validity of our binding and fission assays, we first analyzed dynamin functions on highly anionic DOPS-containing membranes. Membrane binding was tested using a Proximity-based Labeling of Membrane Associated Proteins (PLiMAP) assay (24, 25). In this assay, liposomes contain 1 mol% of a bifunctional fluorescent crosslinking lipid. Membrane binding brings the protein in proximity of the bifunctional lipid, which upon UV exposure becomes crosslinked with the lipid. Samples are then resolved using SDS-PAGE, and binding can be analyzed by measuring lipid fluorescence associated with the protein. PLiMAP assays revealed strong binding of both Dyn1 and Dyn1(F579A) to DOPS liposomes (*SI Appendix*, Fig. S3*B*). Furthermore, membrane binding caused robust stimulation in

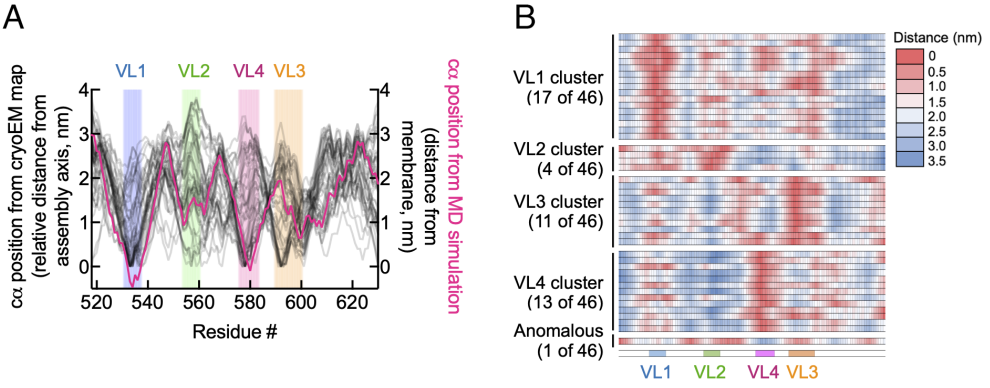

Fig. 1. Structural modeling of the PHD. (*A*) Plots showing the distance of cα atoms in the 518 to 630 residues of the PHD from the axis of assembly. Gray profiles show distances of 46 dynamin PHDs in the cryo-EM map of the membrane-bound dynamin polymer. Distances shown are relative, with the distance of the residue closest to the axis of assembly defined as zero. Magenta profile shows the cα atom distances obtained from previous MD simulations of the PHD on a planar membrane (14). Zero marks the position of the phosphate plane of the membrane. (*B*) Relative distances of cα atoms from structural modeling shown as a heat map.

their GTPase activities (*SI Appendix*, Fig. S3*C*). On supported membrane templates (SMrTs), which comprise an array of membrane nanotubes supported on polyethylene glycol (PEG) cushions (12, 26), addition of Dyn1(F579A) with GTP caused fission and severing of nanotubes, just like Dyn1 (*SI Appendix*, Fig. S3*D* and Movie S1). Together, these results rule out any global effects on protein function caused by reducing VL4 loop hydrophobicity.

Due to the sensitive fluorescence-based read-out, PLiMAP is particularly useful in testing binding of proteins to liposomes containing low and physiologically relevant concentrations of lipids. On liposomes containing 1 mol% 1,2-dioleoyl-sn-glycero-3-phospho-(1′-myo-inositol-4′,5′-bisphosphate) ($PI(4,5)P_2$) and 15 mol% DOPS, Dyn1 bound these membranes with an apparent affinity (K_d) of ~200 nM, which is consistent with previous estimates (22). Under these stringent conditions, Dyn1(F579A) showed substantial defects with a significantly lower binding affinity (K_d ~ 560 nM) and a 2.6-fold lower maximal binding (B_{max}) (Fig. 2 *A* and *B*). While a reduction in binding affinity is consistent with the role of the VL4 in membrane anchoring, a reduction in B_{max} was unexpected and we investigated the cause for this effect. Previous reports analyzing binding of peripheral membrane proteins have indicated that while the K_d reflects the strength of interaction between specific residues on the protein with lipids, the B_{max} depends on abundance of both the interacting lipid and membrane defects that facilitate insertion of hydrophobic residues in proteins (27). Furthermore, membrane defects are more abundant on membranes of high curvature (28). MD simulations reveal that unlike VL1, VL4 does not directly interact with $PI(4,5)P_2$ (14) and we wondered if the ability of VL4 to insert into membrane defects could allosterically stabilize dynamin on the membrane. If this was the case, then the F579A mutation could render dynamin binding more sensitive to membrane curvature. To test this, we turned to a spatially resolved microscopic assay that monitors protein binding to membrane nanotubes of different sizes (and hence curvatures) in SMrTs. We have earlier confirmed that $PI(4,5)P_2$ is uniformly distributed on membrane nanotubes of varying sizes (12), which should allow us to specifically test the influence of membrane curvature on protein binding. SMrTs were incubated with fluorescently labeled dynamin for 15 min, washed with buffer and imaged. Dyn1 binding and self-assembly caused it to organize as numerous foci on every nanotube (Fig. 2*C*). In contrast, Dyn1(F579A) formed substantially fewer foci, which were only found on some tubes (Fig. 2*C*). Because of this stochasticity in binding, we correlated the probability of detecting a dynamin focus on a nanotube to its radius. For Dyn1, such binding probability showed a shallow dependence on the starting tube size (Fig. 2*D*). In contrast, Dyn1(F579A) was severely defective with significantly lower binding even on highly curved tubes and a sharp decline in binding on wider tubes (Fig. 2*D*). Importantly, these attributes were also seen with the CMT-linked mutant M580T located in VL4 (Fig. 2 *C* and *D*). Consistent with the trend seen with membrane binding (Fig. 2*D*), addition of Dyn1 with GTP showed robust fission of nanotubes of a wide range of sizes, while the VL4 mutants showed severe defects in fission, with tubes thinner than 15 nm radius showing a fractional fission probability and tubes wider than 20 nm radius showing no fission (Fig. 2*E*). Thus, reducing VL4 hydrophobicity causes dynamin functions to become acutely sensitive to membrane curvature. Membrane binding and assembly stimulated GTPase activity of the ubiquitously expressed Dyn2 is more sensitivity to membrane curvature (16). Indeed, Dyn2's fission activity showed a steep dependence on membrane curvature with tubes thinner than 20 nm radius showing a fractional fission probability and tubes wider than 20 nm showing no fission, which was not the case for Dyn1 (Fig. 2 *E* and *F*). The VL4 mutations in Dyn2 manifested in severe defects with fission activity being completely abolished on tubes of all sizes. Thus, reducing VL4 hydrophobicity has more profound effects on Dyn2 than Dyn1.

To assess potential roles of the VL4 in dynamin functions beyond membrane binding, we raised the $PI(4,5)P_2$ concentration to 5% to facilitate Dyn1(F579A) binding and turned to stage-specific reconstitution of the fission reaction. Dyn1 foci seen on SMrTs represent scaffolds that constrict the underlying tube (Fig. 2*C*). This is apparent from the dimmer membrane fluorescence seen under Dyn1 foci (*SI Appendix*, Fig. S4*A*). Flowing GTP causes further constriction of the scaffolded tube to a prefission intermediate before fission (*SI Appendix*, Fig. S4*B*). Based on a calibration procedure that equates membrane fluorescence to tube size (26), we find the Dyn1 scaffolded tube radius to be 9.9 ± 1.3 nm (mean ± SD) and the prefission tube radius to be 5.5 ± 1.0 nm (Fig. 2*G*), which is consistent with our earlier estimates (12). In contrast, the Dyn1(F579A) scaffolded tube radius was 7.5 ± 1.8 nm, which is significantly lower than seen with Dyn1. This indicates that VL4 restrains dynamin's ability to constrict such that when mutated, the scaffold constricts tubes to a thinner dimension. Furthermore, the prefission tube radius was 3.6 ± 0.9 nm, which is significantly lower than seen with Dyn1. The VL4 therefore facilitates fission because when mutated, tubes must constrict to a greater extent for fission. To test if these effects are specific to VL4, we analyzed the VL1 mutant Dyn1(I533A) on 5% $PI(4,5)P_2$-containing membranes. Surprisingly, the VL1 mutant showed a wider scaffolded tube radius of 13.8 ± 2.1 nm and a wider prefission tube radius of 6.4 ± 1.4 nm. VL1 therefore exerts an opposite influence on dynamin functions compared to VL4. Unlike VL4, VL1 facilitates tube constriction but negatively impacts fission. Together, our results highlight contrasting roles of the VL on dynamin functions.

Reconstituting Dynamin Functions on Physiologically Relevant Membrane Templates. The above-described assays are quite minimal in the sense that they rely solely on dynamin's ability to bind lipids for membrane recruitment. In cells, dynamin relies on multivalent interactions with lipids and endocytic proteins. The PHD binds $PI(4,5)P_2$, while the PRD binds a host of SH3 domains in endocytic proteins, which together facilitate dynamin's recruitment to the membrane. To recreate such multivalent interactions, we tried recruiting dynamin binding partner proteins on SMrTs. Our attempts with Dyn1 partners like amphiphysin1 and endophilin were unsuccessful because they showed negligible binding to SMrTs containing 1 mol% $PI(4,5)P_2$ and 15 mol% DOPS. We then turned to Amphiphysin2 or BIN1 (bridging-interactor 1), specifically isoform eight which contains a positively charged PI stretch that binds $PI(4,5)P_2$ with high affinity, and an SH3 domain that interacts with dynamin and also participates in CME as a dynamin binding partner (29–32).

Flowing BIN1-GFP onto SMrTs containing 1 mol% $PI(4,5)P_2$ and 15 mol% DOPS caused it to readily bind nanotubes. BIN1-GFP appeared uniformly distributed on some nanotubes (see box with dotted line and associated fluorescence profiles in Fig. 3*A*), while on others, it was organized as discrete foci (box with solid line and associated fluorescence profiles in Fig. 3*A*). These foci coincided with lower membrane fluorescence, implying constriction of the underlying tube. BIN1 is widely known for its ability to tubulate planar membranes (31). But a tendency for it to organize into membrane active scaffolds on tubes has not been reported. We therefore investigated this phenomenon. The coefficient of

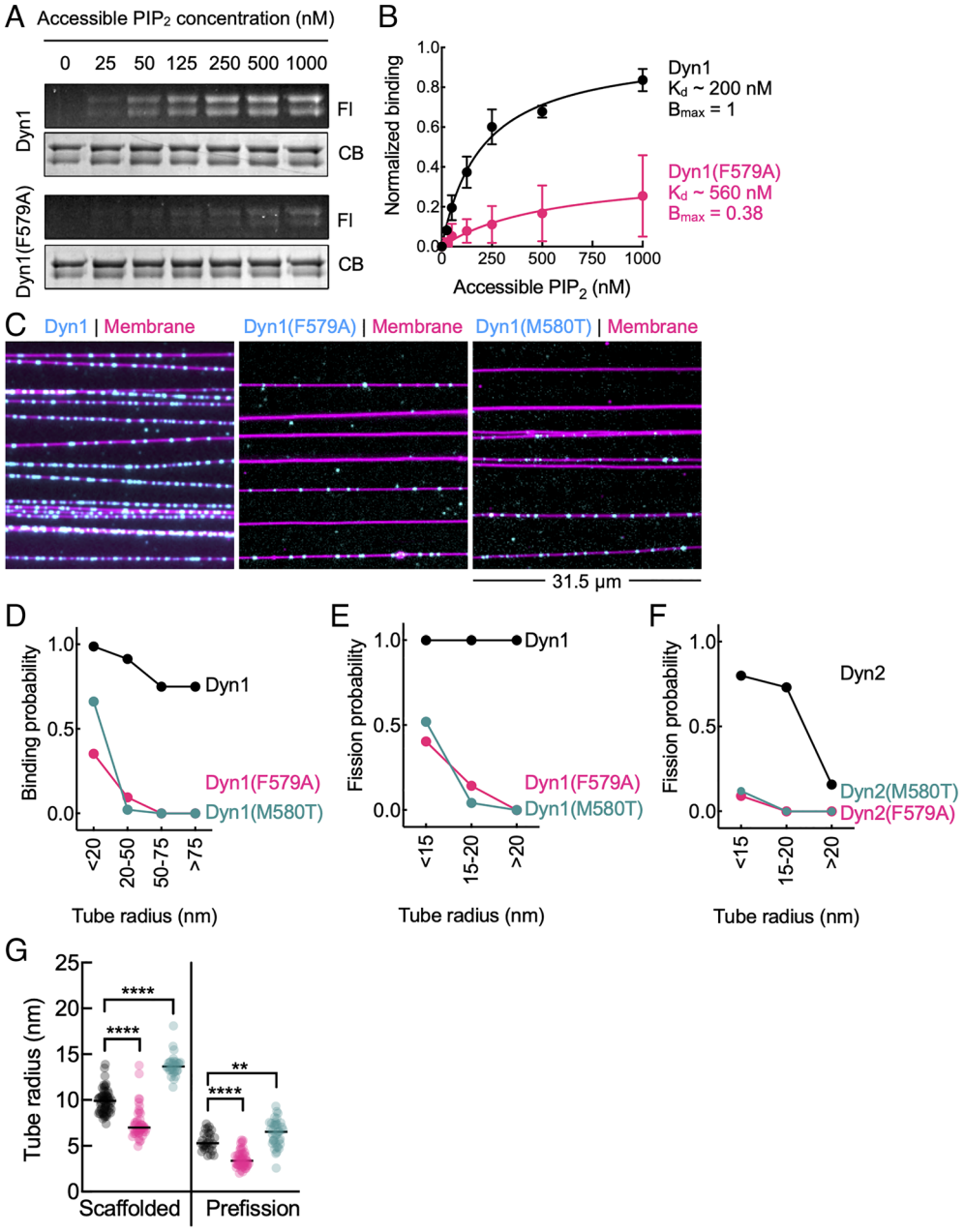

Fig. 2. Role of VL4 in dynamin functions assayed on membranes with physiological lipid composition. (*A*) Results from a representative PLiMAP experiment showing in-gel fluorescence (Fl) and Coomassie brilliant blue (CB) staining of Dyn1 (black) and Dyn1(F579A) (magenta) on 1 mol% PI(4,5)P_2 and 15 mol% DOPS liposomes. (*B*) Quantitation of PLiMAP data and fits to a one-site binding isotherm. Data represent the mean ± SD of three independent experiments. (*C*) Representative micrographs showing the distribution of fluorescent Dyn1, Dyn1(F579A), and Dyn1(M580T) (all cyan) on SMrTs (magenta). (*D*) Binding probabilities of Dyn1 (black), Dyn1(F579A) (magenta), and Dyn1(M580T) (green) as a function of tube radius. For Dyn1, number of tubes analyzed were 231 (<20 nm), 138 (20 to 50 nm), 20 (50 to 75 nm), and 48 (>75 nm). For Dyn1(F579A), number of tubes analyzed were 71 (<20 nm), 179 (20 to 50 nm), 28 (50 to 75 nm), and 10 (>75 nm). For Dyn1(M580T), number of tubes analyzed were 62 (<20 nm), 91 (20 to 50 nm), 10 (50 to 75 nm), and 2 (>75 nm). (*E*) Fission probabilities of Dyn1 (black), Dyn1(F579A) (magenta), and Dyn1(M580T) (green) as a function of tube radius. For Dyn1, number of tubes analyzed were 51 (<15 nm), 16 (15 to 20 nm), and 7 (>20 nm). For Dyn1(F579A), a number of tubes analyzed were 52 (<15 nm), 7 (15 to 20 nm), and 4 (>20 nm). For Dyn1(M580T), number of tubes analyzed were 131 (<15 nm), 24 (15 to 20 nm), and 24 (>20 nm). (*F*) Fission probability with Dyn2 (black), Dyn2(F579A) (magenta), and Dyn2(M580T) (green) as a function of tube radius. For Dyn2, number of tubes analyzed were 90 (<15 nm), 26 (15 to 20 nm), and 19 (>20 nm). For Dyn2(F579A), number of tubes analyzed were 11 (<15 nm), 21 (15 to 20 nm), and 71 (>20 nm). For Dyn2(M580T), number of tubes analyzed were 50 (<15 nm), 14 (15 to 20 nm), and 20 (>20 nm). (*G*) Scaffolded and prefission tube radii with Dyn1 (black), Dyn1(F579A) (magenta) and Dyn1(I533A) (green). Data represent estimates from 58 scaffolds and 28 prefission intermediates for Dyn1, 44 scaffolds and 45 prefission intermediates for Dyn1(F579A), and 25 scaffolds and 38 prefission intermediates for Dyn1(I533A). Statistical significance was estimated using Mann–Whitney's test where **** denotes $P < 0.0001$ and ** denotes $P = 0.005$.

variation (COV) of BIN1-GFP fluorescence along the length of the tube reports on the non-uniformity in BIN1 distribution. The COV showed a rise with an increase in tube radius (Fig. 3*B*). Conversely, BIN1-GFP membrane density, which is the average BIN1-GFP fluorescence divided by the average membrane fluorescence, showed a decline with an increase in tube radius (Fig. 3*C*). Together, these results indicate that an increase in tube size converts BIN1 organization from a long and continuous scaffold into small and discrete units, likely because of limiting protein density on the membrane. Correlating the tube radius under BIN1 scaffolds to the starting tube radius clearly reveals the constriction activity of BIN1. Thus, tubes of ~10 nm starting radius retain their dimension, while tubes of ~30 nm radius get constricted to ~12 nm (Fig. 3*D*). These estimates agree well with the

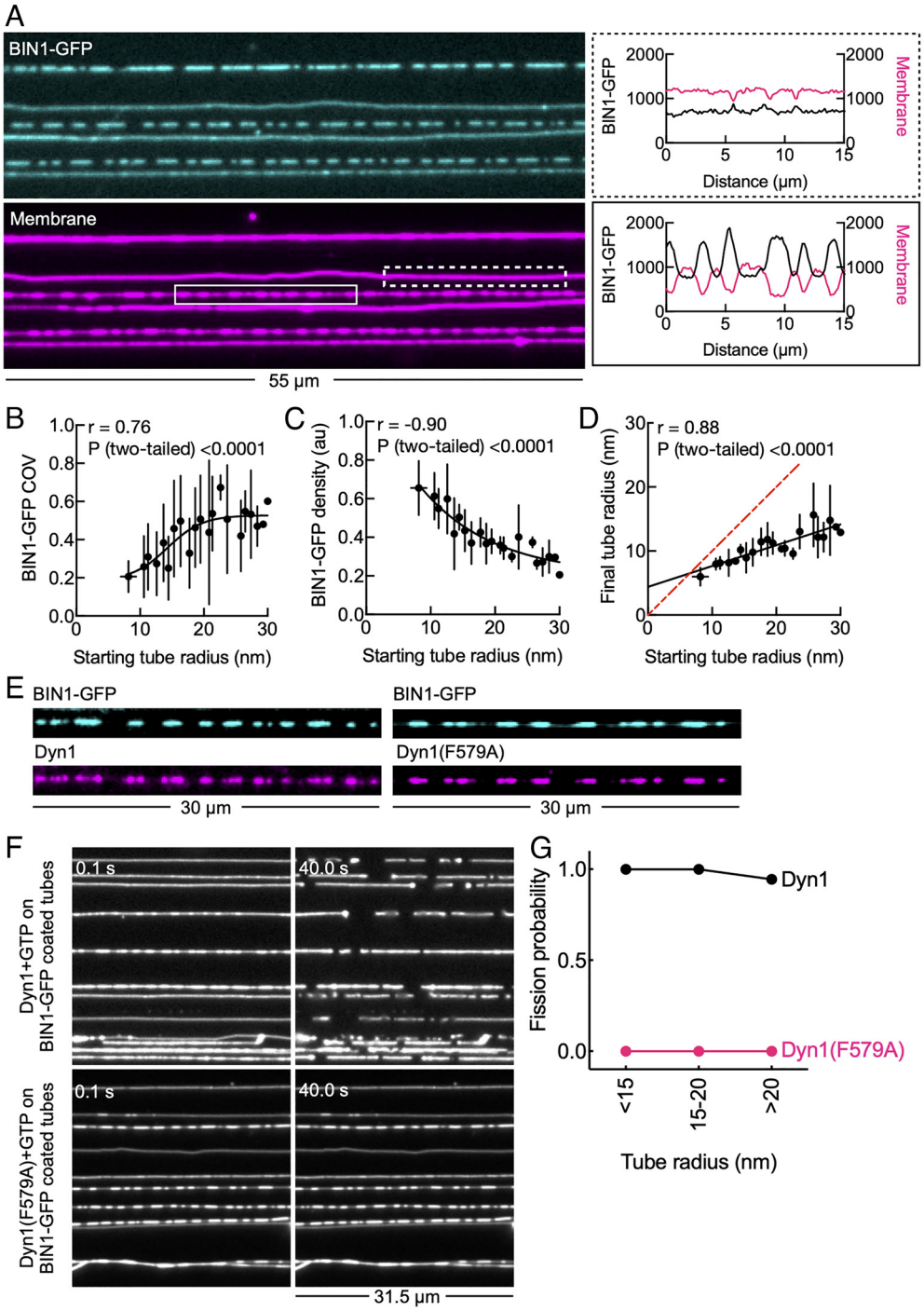

Fig. 3. Dynamin functions analyzed on BIN1-coated membrane nanotubes. (*A*) A representative micrograph showing the distribution of BIN1-GFP (cyan) on SMrTs (magenta). (*B*) Coefficient of variation (COV) of BIN1-GFP fluorescence as a function of tube radius. (*C*) BIN1-GFP density as a function of tube radius. (*D*) Final tube radius under BIN-GFP scaffolds as a function of the starting tube radius. The red dotted line represents a scenario without tube constriction. Data in *B*–*D* represent the mean ± SD with the starting tube radius estimates binned to their integral values. (*E*) Representative fluorescence micrographs of SMrTs showing localization of Dyn1 and Dyn1(F579A) (both magenta) on BIN1-GFP (cyan) scaffolds. (*F*) Representative fluorescence micrographs showing the effect of addition of Dyn1 and Dyn1(F579A) with GTP to BIN1-coated membrane nanotubes. (*G*) Fission probabilities with Dyn1 (black) and Dyn1(F579A) (magenta) as a function of starting tube radius. For Dyn1, number of tubes analyzed were 9 (<15 nm), 6 (15 to 20 nm), and 18 (>20 nm). For Dyn1(F579A), number of tubes analyzed were 34 (<15 nm), 2 (15 to 20 nm), and 1 (>20 nm).

limiting value of 14 nm reported from cryo-EM measurements of large vesicles tubulated by BIN1 (33). However, the scaffolded tube radius shows a shallow dependence on the starting tube radius (Fig. 3*D*), which implies that BIN1 scaffolds display some degree of plasticity and adapt to the dimensions of the underlying tube. Based on these attributes, BIN1-coated membrane nanotubes should represent ideal templates to interrogate dynamin functions in a more native context. BIN1 scaffolds represent sites of high local density of SH3 domains and their ability to constrict tubes of a wide range of sizes to a narrow range of 8 to 14 nm radius would be expected to rescue the acute membrane curvature dependence seen with Dyn1(F579A) in membrane binding and fission.

To confirm if dynamin binds BIN1 via SH3-PRD interactions on membrane nanotubes, especially because of the partial C-terminal truncation of the PRD seen in our recombinant

dynamin preparations (*Materials and Methods*), we prepared BIN1-GFP-coated membrane nanotubes and flowed in fluorescent dynamin. Dynamin fluorescence coincided with BIN1-GFP fluorescence implying efficient binding (Fig. 3*E*). Thus, the partial C-terminal truncation of the PRD appears not to significantly impact dynamin's ability to engage with BIN1's SH3 domain. We then assayed for dynamin functions in the presence of GTP on BIN1-coated membrane nanotubes. For these experiments, we monitored only the membrane fluorescence channel to improve temporal resolution and because our results confirm that BIN1 is either distributed uniformly on narrow membrane tubes or is localized as discrete scaffolds, each of which coincides with dimmer tube fluorescence (Fig. 3*A*). Flowing Dyn1 with GTP on BIN1-coated membrane nanotubes showed fission. Fission was apparent on nanotubes that were uniformly coated with BIN1 as well as on those displaying localized BIN1-dependent constrictions (Fig. 3*F*). Bulk fission kinetics, estimated by scoring the number of cuts seen with time across several tubes in the microscope field of view, was a bit slower on BIN1-coated tubes (~1.5 cuts.s^{-1}) than seen on tubes without BIN1 (4.7 cuts.s^{-1}), possibly because the presence of BIN1 reduces the freely available PI(4,5)P_2 required for engaging dynamin. On tubes showing localized BIN1-dependent constrictions, time-lapse imaging revealed that fission took place within the BIN1 scaffold, which is evident from the dimmer constricted region undergoing splitting (*SI Appendix*, Fig. S5 and Movie S2). Remarkably, flowing Dyn1(F579A) with GTP showed no fission of BIN1-coated membrane nanotubes (Fig. 3*F* and Movie S2). Indeed, correlating fission probability to the starting tube size revealed this mutant to be fission-defective across a range of tube sizes (Fig. 3*G*).

VL4 Mutants with Reduced Hydrophobicity Are Defective in Cellular Functions. Finally, we tested the VL4 mutants in a cellular assay for dynamin functions. Dynamin's ability to sustain CME has been monitored using clathrin-dependent uptake of transferrin. During late stages of clathrin-mediated endocytosis, dynamin is recruited to the necks of clathrin-coated pits to catalyze fission leading to the release of clathrin-coated vesicles (29). Expression of GTPase-, self-assembly, and membrane binding-defective dynamin mutants causes the arrest of transferrin uptake by dominant-negative inhibition of native dynamin function (34–36). This experimental paradigm is also relevant to understand potential CMT-linked mutations since these are autosomal dominant. We tested the importance of VL4 by monitoring transferrin uptake in cells overexpressing VL4 mutants. These assays were carried out in dynamin2 KO HeLa cells to specifically test dynamin1 functions. As a control, overexpressing the GTPase-defective Dyn1(K44A)-GFP mutant significantly reduced transferrin uptake compared to cells expressing Dyn1-GFP (34) (Fig. 4 *A* and *B*). Importantly, overexpressing Dyn1(F579A)-GFP and the CMT-linked mutant Dyn1(M580T)-GFP also showed a significant reduction in transferrin uptake (Fig. 4 *A* and *B*). This is apparent from loss of the intense perinuclear fluorescence of transferrin seen in cells expressing the mutant compared to non-transfected cells (Fig. 4*A*) and a quantitative reduction in transferrin fluorescence associated with cells (Fig. 4*B*). These results corroborate data from in vitro assays showing a defect in membrane fission and signify the importance of VL4 for dynamin functions. However, effects on CME upon overexpressing the VL4 mutants were not as severe as that seen with Dyn1(K44A), possibly explaining why the CMT-linked mutation is debilitating but not lethal.

Discussion

Recent MD simulations show that VL1 and VL4 loops stabilize the PHD on the membrane (14). While the significance of VL1 has been established (11, 13), the present work is the first to experimentally address the importance of VL4 to dynamin functions. We carried out structural modeling of the PHD in the cryo-EM map of the membrane-bound dynamin1 polymer. The modeled data are quite consistent with simulations, barring some aspects which could be attributed to differences in membrane composition and curvature and the low resolution of PHDs in the cryo-EM map. The modeled data show that VL4 is the next preferred membrane-inserting anchor after VL1 and together stabilizes dynamin on the membrane.

The importance of VL4 to dynamin's membrane binding and fission is apparent from the detrimental effects seen with mutants that reduce its hydrophobicity. In bulk liposome-based assays, the VL4 mutant displays significant defects in binding to membranes containing physiologically relevant levels of PI(4,5)P_2. Extending such analysis to assays on membrane nanotubes, we find that VL4 mutants render Dyn1 and 2 binding more sensitive to membrane curvature. Interestingly, simulations of the F579A mutant in the isolated PHD showed no apparent defect in membrane binding. This discrepancy is likely because membrane dissociation would

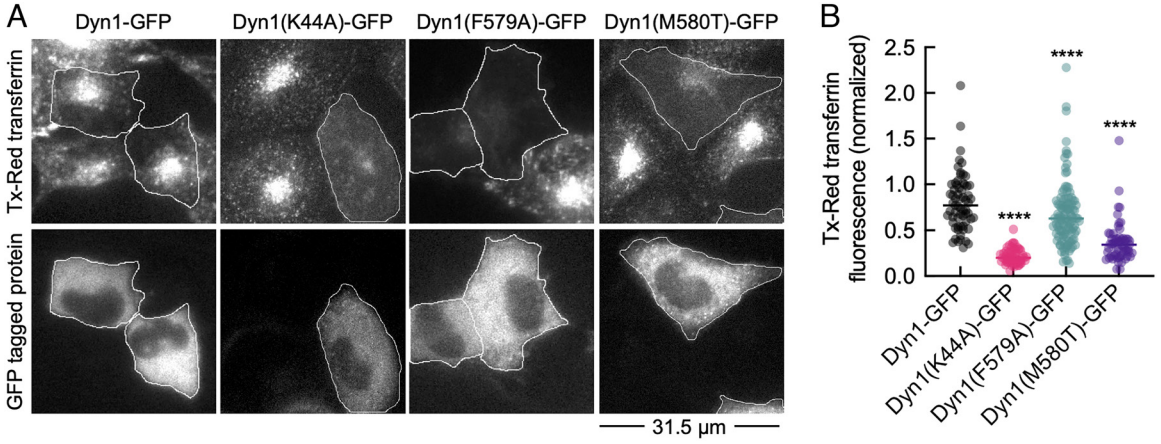

Fig. 4. Overexpression of VL4 mutants cause defects in clathrin-mediated endocytosis. (*A*) Representative micrographs showing uptake of fluorescent transferrin in dynamin2 KO HeLa cells expressing Dyn1-GFP and its mutants. (*B*) Tx-Red transferrin uptake in cells expressing Dyn1-GFP (n = 84), Dyn1(K44A)-GFP (n = 57), Dyn1(F579A)-GFP (n = 109), and Dyn1(M580T)-GFP (n = 58). Data were normalized to the mean transferrin fluorescence seen in non-transfected cells for each condition. Significance was estimated using Mann–Whitney's test where **** denotes $P < 0.0001$.

be favored in the full-length protein than with an isolated PHD such that a subtle reduction in the hydrophobicity of VL4 could change membrane partitioning properties more significantly for the full-length protein than the isolated PHD. Dynamin self-assembles into helical scaffolds, and its binding is inherently favored on membranes of high curvature (37). But dynamin scaffolds constrict tubes thereby extending the range of curvatures that can support binding and self-assembly. Our results indicate that VL4 contributes to this process since when mutated, dynamin shows a steep decline in binding with a decrease in membrane curvature. However, on tubes of a size range that can recruit the VL4 mutants, addition of these mutants with GTP caused fission indicating that these mutants are partially defective in function.

The PHD actively facilitates membrane fission. This is evident from our previous work showing that replacing the native PHD-$PI(4,5)P_2$ interaction with a generic 6xHis-chelator lipid interaction or with a polylysine-PS interaction in dynamin supports fission but with slower kinetics and with the presence of long-lived highly constricted tubular intermediates (38). This is likely because VL insertion has been shown to facilitate non-bilayer like arrangements of membrane lipids and lower the membrane bending energy (13, 14, 39). Our results extend these models and reveal that the VLs exert distinct and separable effects on dynamin function. The VLs display a moderate degree of exclusivity in orientation. This is apparent from the fact that the modeled PHDs can be categorized into separate clusters based on which VL inserts into the membrane. This could signify negative allostery whereby insertion of one VL inhibits insertion of another through a yet unidentified relay mechanism. Such selectivity is also apparent in how they affect dynamin's constriction and fission activities. Comparative analysis of VL1 and VL4 mutants reveals that VL1 facilitates while VL4 restrains the dynamin scaffold from constricting tubes. Furthermore, fission with dynamin is achieved when tubes constrict to a ~5.5 nm radius prefission intermediate. But with the VL1 mutant, fission is attained with a wider ~6.4 nm radius intermediate. This indicates the VL1 negatively impacts the fission process. In contrast, fission with the VL4 mutant manifests when tubes constrict to a thinner ~3.5 nm radius intermediate, indicating that VL4 catalyzes fission. MD simulations of the PHD reveal that the F579A mutation causes VL1 to insert more deeply into the membrane, while the I533A mutation has no effect on the VL4 (14). That fission with the VL4 mutant requires a greater extent of constriction could arise from a deeper insertion of VL1.

We expected that defects in membrane binding and fission with Dyn1(F579A) would be rescued by involving SH3-PRD interactions. BIN1 scaffolds are expected to facilitate dynamin functions. They represent sites with a high local concentration of SH3 domains and, based on results presented here, also constrict tubes to a fission-compliant size. Previous reports have indicated that a stoichiometric excess of BAR domain proteins such as endophilin and amphiphysin can inhibit dynamin functions, likely by forming mixed scaffolds that prevent dynamin's G domain interactions that are necessary for stimulated GTPase activity (40, 41). Our assays are designed to allow BIN1 to first form scaffolds and then recruit dynamin. Washing off excess BIN1 before dynamin addition could have ensured that dynamin self-assembles within the BIN1 scaffold to cause fission. Such sequential addition more closely mimics the cellular scenario wherein endocytic proteins arrive before dynamin for fission of clathrin-coated pits (7, 29), although alternate models of a cooperative but not sequential recruitment of endocytic proteins and dynamins have been proposed (8). Dyn1(F579A) binds BIN1 scaffolds but surprisingly fails at fission. BIN1 scaffolds compete with dynamin for $PI(4,5)P_2$ binding, and the lower affinity of Dyn1(F579A) for $PI(4,5)P_2$ could affect its ability to actively engage with the membrane. This emphasizes a general principle wherein endocytic partner proteins act in a mutually competing manner. Partner protein interactions facilitate dynamin's recruitment, but the same partners could compete with dynamin's engagement with the membrane. Consequently, subtle defects in membrane binding could become amplified within the local microenvironment of the BIN1 scaffold thus rendering the VL4 mutant defective in fission and CME.

The PHD is a hotspot for mutations that cause several genetic disorders. Many of the mutations reside in regions that are highly conserved across all isoforms of dynamin. Our work extends these observations by characterizing functions of the VL4 in dynamin. Our results therefore emphasize the importance of this novel VL4 membrane anchor in dynamin functions and reveal how finely tuned lipid–protein interaction have evolved to facilitate dynamin functions in membrane fission and CME.

Materials and Methods

Structural Modeling of the PHD. Due to the low (>7 Å) resolution of the PHDs in the cryo-EM map, we used a combination of global search and local fitting approaches to maximize fits of dynamin dimers in the cryoEM electron density map of the membrane-bound Dyn1ΔPRD polymer (23). For this, dynamin dimers were first identified in the electron density map using ADP_EM (42), which is a rigid-body fitting tool that uses spherical harmonics-based approaches to accelerate the search. Following this, we maximized fits of individual dynamin dimers through iterative modeling using iMODFIT (43). Only the PHDs were found adjusting through the iterations. Each of the two PHDs in the dimer is capable of separately converging to their best fits in terms of orientation, which provided us with 46 independent orientations in the polymer. In four of the 46 cases, the residue that showed the highest proximity to the membrane was located adjacent to the VL boundary. In these cases, we considered the next most proximal residue located within the VL boundary.

Constructs and Plasmids. Human dynamin1 and BIN1-EGFP (isoform 8) (Addgene plasmid #27305) were cloned in pET15b with N-terminal 6xHis and C-terminal StrepII tags. Human dynamin 2 was cloned in pET15B with a C-terminal StrepII tag. Mutations were introduced using PCR. For mammalian cell expression, human dynamin1 and its mutants were cloned with a C-terminal GFP fusion into pcDNA3.0. All clones were confirmed by sequencing.

Protein Purification and Fluorescent Labeling. Proteins were expressed in BL21(DE3) cells grown in autoinduction medium at 18 °C for 36 h. Bacterial cells were pelleted and stored at −40 °C. The frozen bacterial pellet was thawed in 20 mM HEPES pH 7.4, 500 mM NaCl with a protease inhibitor cocktail (Roche) and lysed by sonication in an ice-water bath. Lysate was spun at 30,000 g for 20 min. For proteins containing the 6xHis and StrepII tags (dynamin1 and BIN1-GFP), the supernatant was incubated with HisPur™ Cobalt Resin (Thermo Fisher Scientific). The resin was washed with 20 mM HEPES pH 7.4, 500 mM NaCl and bound protein was eluted with 20 mM HEPES pH 7.4, 500 mM NaCl, and 100 mM EDTA. The elution was loaded onto a StrepTrap HP column (GE Lifesciences), washed with 20 mM HEPES pH 7.4, 150 mM NaCl, and eluted with the same buffer containing 2.5 mM desthiobiotin. Despite this two-step purification procedure, dynamin1 elutes with a partial C-terminal truncation because it exists as a tetramer (38). For dynamin2, the supernatant was loaded onto a StrepTrap HP column, washed with 20 mM HEPES pH 7.4, 500 mM NaCl, 100 mM EDTA, exchanged for 20 mM HEPES pH 7.4, 150 mM NaCl, and eluted with the same buffer containing 2.5 mM desthiobiotin. Proteins were spun at 100,000 g to remove aggregates before use in assays. Protein concentration was estimated from UV absorbance at 280 nm using the molar extinction coefficient predicted by the Expasy ProtParam tool. Dynamin was labeled with fivefold excess of Alexa488 C5-maleimide or Alexa594 C5-maleimide (Invitrogen) in 20 mM HEPES pH 7.4, 150 mM NaCl. The reaction was quenched with excess dithiothreitol, and the unreacted dye was removed by extensive dialysis.

Liposome Preparation. 1,2-dioleoyl-sn-glycero-3-phosphocholine (DOPC), 1,2-dioleoyl-sn-glycero-3-phospho-L-serine (sodium salt), (DOPS), and 1,2-dioleoyl-sn-glycero-3-phospho-(1′-myo-inositol-4′,5′-bisphosphate)

(ammonium salt) ($PI(4,5)P_2$) were from Avanti Polar Lipids. The UV-activable, diazirine-containing fluorescent lipid probe BODIPY-diazirine phosphatidylethanolamine (BDPE) was prepared as described earlier (24, 25). Lipids were aliquoted at desired ratios in a glass tube and dried under high vacuum for 30 min to a thin film. Deionized water was added to the dried lipids to achieve a final concentration of 1 mM. Lipids were hydrated at 50 °C for 30 min, vortexed vigorously and extruded through 100 nm pore-size polycarbonate filters (Whatman).

GTPase Assays. For GTPase assays, dynamin (0.1 μM) was incubated with DOPS liposomes (10 μM) in 20 mM HEPES pH 7.4, 150 mM KCl containing 1 mM GTP (Jena Bioscience) and 1 mM $MgCl_2$. The released inorganic phosphate was measured using a malachite green-based colorimetric assay (38, 44).

Proximity-Based Labeling of Membrane-Associated Proteins (PLiMAP). PLiMAP was carried out as described earlier (24, 25). Briefly, liposomes containing 1 mol% of BDPE were incubated with dynamin at a 100:1 lipid:protein molar ratio in a final volume of 30 μL. The reaction was incubated in the dark at room temperature for 30 min and exposed to 365 nm UV light (UVP crosslinker CL-1000L) at an intensity of 200 mJ cm^{-2} for 1 min. The reaction was mixed with sample buffer, boiled, and resolved using SDS-PAGE. Gels were first imaged for BODIPY fluorescence on an iBright1500 (Thermo Fischer Scientific) and later fixed and stained with Coomassie Brilliant Blue (CB). Binding data were fitted to a one-site binding isotherm using Graphpad Prism.

Supported Membrane Templates (SMrT). Supported membrane templates (SMrT) were prepared as described earlier (26). Briefly, lipids were aliquoted at desired ratios to a final concentration of 1 mM in chloroform. The lipid mixes also contained the fluorescent lipid *p*Texas-Red DHPE (Thermo Fisher Scientific) at 1 mol% concentration. 2 μL of the lipid mix was spread with a glass syringe on a PEGylated glass coverslip, dried, and assembled inside an FCS2 flow chamber (Bioptechs). The chamber was filled with 20 mM HEPES pH 7.4, 150 mM NaCl and flowed at high rates to form SMrTs. For binding, 0.3 μM dynamin was flowed onto SMrTs in 20 mM HEPES pH 7.4, 150 mM NaCl and incubated for 10 min. Templates were imaged after washing off excess dynamin. For fission, SMrTs were pre-equilibrated with an oxygen scavenger cocktail in 20 mM HEPES pH 7.4, 150 mM NaCl and time-lapse images were acquired while flowing in 0.3 μM dynamin mixed with 1 mM GTP (Jena Bioscience) and 1 mM $MgCl_2$ in 20 mM HEPES pH 7.4, 150 mM NaCl. For experiments involving BIN1, 0.2 μM of BIN1-GFP was flowed onto SMrTs, incubated for 10 min and unbound protein was washed off before flowing in dynamin with or without GTP.

Cell Culture and Transferrin Uptake Assay. Dynamin2 KO HeLa cells have been reported earlier (45). Cells were cultured in complete DMEM with 10% FBS and 1% penicillin-streptomycin (HiMedia) and maintained at 37 °C in humidified 5% CO_2. Cells were transfected with dynamin using Lipofectamine 2000 (Thermo Fisher Scientific). Transfected cells were trypsinized and plated on 40 mm glass coverslips (Bioptechs). Transferrin uptake experiments were performed between 24 and 48 h post-transfection. Cells were serum-starved for 2 h in serum-free DMEM, and the coverslips were assembled in an FCS2 chamber maintained at 37 °C. The media was exchanged for HEPES-buffered Hank's balanced salt solution, and cells were fed with 50 μg mL^{-1} of Texas Red-labeled transferrin (Invitrogen) and incubated for 10 min. Excess transferrin was washed off before imaging the cells.

Fluorescence Imaging and Image Analysis. SMrT templates and cells were imaged through 100× or 60×, 1.4 NA oil-immersion objectives, respectively, on an Olympus IX83 inverted microscope connected to an LED light source (CoolLED) and an Evolve 512 EMCCD camera (Photometrics). Image acquisition was controlled by μManager, and images were analyzed using Fiji (46). Tube sizes were estimated based on a calibration procedure as described earlier (26). Binding probability was calculated by estimating the fraction of tubes that showed at least one foci of dynamin. Fission probability was calculated by estimating the fraction of tubes that showed at least one cut. Transferrin uptake was quantitated by recording the maxima and minima of Tx-Red transferrin fluorescence intensities in region-of-interest (ROIs) marking cells. The minima were subtracted from the maxima to get background-corrected intensities. These intensities were further correct for autofluorescence from cells not fed with transferrin. Background-corrected intensities in transfected cells were normalized to the median intensity in non-transfected cells in each experiment. This was necessary to correct for differences in Tx-Red transferrin fluorescence intensities across experiments.

Data, Materials, and Software Availability. Code data have been deposited at the codesrivastavalab server (https://github.com/codesrivastavalab/cryoEM-dynPHD). All study data are included in the article and/or *SI Appendix*.

ACKNOWLEDGMENTS. H.K. and S.B. thank Indian Institute of Science Education and Research, Pune and K.B. thanks Indian Institute of Science, Bengaluru for graduate fellowships. We thank Mike Ryan (Monash University) for the dynamin2 knock-out HeLa cells. A.S. thanks the Department of Science and Technology (DST) for the National Supercomputing Mission grant (DST/NSM/R&D_HPC_Applications/2021/03.10) and the Supercomputing Education and Research Centre at Indian Institute of Science, Bengaluru for the high-performance computing (HPC) resources. A.S. also acknowledges support from the high-performance computing facility "Beagle", setup through a partnership between the Department of Biotechnology and Indian Institute of Science, Bengaluru. T.J.P. thanks the Howard Hughes Medical Institute for funding support. We thank the Pucadyil Lab members for comments on the manuscript.

1. K. Faelber *et al.*, Structural insights into dynamin-mediated membrane fission. *Structure* **20**, 1621–1628 (2012).
2. J. S. Chappie, F. Dyda, Building a fission machine–structural insights into dynamin assembly and activation. *J. Cell Sci.* **126**, 2773–2784 (2013).
3. S. L. Schmid, V. A. Frolov, Dynamin: Functional design of a membrane fission catalyst. *Annu. Rev. Cell Dev. Biol.* **27**, 79–105 (2011).
4. S. M. Ferguson, P. D. Camilli, Dynamin, a membrane-remodelling GTPase. *Nat. Rev. Mol. Cell Biol.* **13**, 75–88 (2012).
5. B. Antonny *et al.*, Membrane fission by dynamin: What we know and what we need to know. *EMBO J.* **35**, 2270–2284 (2016).
6. M. Mettlen, T. Pucadyil, R. Ramachandran, S. L. Schmid, Dissecting dynamin's role in clathrin-mediated endocytosis. *Biochem. Soc. Trans.* **37**, 1022 (2009).
7. O. Daumke, A. Roux, V. Haucke, BAR domain scaffolds in dynamin-mediated membrane fission. *Cell* **156**, 882–892 (2014).
8. M. Meinecke *et al.*, Cooperative recruitment of dynamin and BIN/amphiphysin/Rvs (BAR) domain-containing proteins leads to GTP-dependent membrane scission. *J. Biol. Chem.* **288**, 6651–6661 (2013).
9. K. M. Ferguson, M. A. Lemmon, J. Schlessinger, P. B. Sigler, Crystal structure at 2.2 A resolution of the pleckstrin homology domain from human dynamin. *Cell* **79**, 199–209 (1994).
10. M. A. Lemmon, K. M. Ferguson, Signal-dependent membrane targeting by pleckstrin homology (PH) domains. *Biochem. J.* **350**, 1–18 (2000).
11. R. Ramachandran *et al.*, Membrane insertion of the pleckstrin homology domain variable loop 1 is critical for dynamin-catalyzed vesicle scission. *Mol. Biol. Cell* **20**, 4630–4639 (2009).
12. S. Dar, S. C. Kamerkar, T. J. Pucadyil, A high-throughput platform for real-time analysis of membrane fission reactions reveals dynamin function. *Nat. Cell Biol.* **17**, 1588–1596 (2015).
13. A. V. Shnyrova *et al.*, Geometric catalysis of membrane fission driven by flexible dynamin rings. *Science* **339**, 1433–1436 (2013).
14. K. Baratam, K. Jha, A. Srivastava, Flexible pivoting of dynamin pleckstrin homology domain catalyzes fission: Insights into molecular degrees of freedom. *Mol. Biol. Cell* **32**, 1306–1319 (2021).
15. S. Züchner *et al.*, Mutations in the pleckstrin homology domain of dynamin 2 cause dominant intermediate Charcot-Marie-Tooth disease. *Nat. Genet.* **37**, 289–294 (2005).
16. Y.-W. Liu *et al.*, Differential curvature sensing and generating activities of dynamin isoforms provide opportunities for tissue-specific regulation. *Proc. Natl. Acad. Sci. U.S.A.* **108**, E234–E242 (2011).
17. A.-C. Durieux, B. Prudhon, P. Guicheney, M. Bitoun, Dynamin 2 and human diseases. *J. Mol. Med.* **88**, 339–350 (2010).
18. J. Haberlová *et al.*, Phenotypic variability in a large czech family with a dynamin 2–associated Charcot-Marie-Tooth neuropathy. *J. Neurogenet.* **25**, 182–188 (2011).
19. G. M. Fabrizi *et al.*, Two novel mutations in dynamin-2 cause axonal Charcot–Marie–Tooth disease. *Neurology* **69**, 291–295 (2007).
20. M. Bitoun *et al.*, A novel mutation in the dynamin 2 gene in a Charcot-Marie-Tooth type 2 patient: Clinical and pathological findings. *Neuromuscular. Disord.* **18**, 334–338 (2008).
21. S. Zuchner *et al.*, Mutations in the pleckstrin homology domain of dynamin 2 cause dominant intermediate Charcot-Marie-Tooth disease: LBS.002. *Neurology* **64**, 1826–1826 (2005).
22. J. A. Kenniston, M. A. Lemmon, Dynamin GTPase regulation is altered by PH domain mutations found in centronuclear myopathy patients. *EMBO J.* **29**, 3054–3067 (2010).
23. L. Kong *et al.*, Cryo-EM of the dynamin polymer assembled on lipid membrane. *Nature* **13**, 1 (2018).
24. G. P. Jose, S. Gopan, S. Bhattacharyya, T. J. Pucadyil, A facile, sensitive and quantitative membrane-binding assay for proteins. *Traffic* **21**, 297–305 (2020).
25. G. P. Jose, T. J. Pucadyil, PLiMAP: Proximity-based labeling of membrane-associated proteins. *Curr. Protoc. Protein Sci.* **101**, e110 (2020).
26. S. Dar, S. C. Kamerkar, T. J. Pucadyil, Use of the supported membrane tube assay system for real-time analysis of membrane fission reactions. *Nat. Protoc.* **12**, 390–400 (2017).
27. N. S. Hatzakis *et al.*, How curved membranes recruit amphipathic helices and protein anchoring motifs. *Nat. Chem. Biol.* **5**, 835–841 (2009).
28. S. Vanni, H. Hirose, H. Barelli, B. Antonny, R. Gautier, A sub-nanometre view of how membrane curvature and composition modulate lipid packing and protein recruitment. *Nat. Commun.* **5**, 4916 (2014).
29. M. J. Taylor, D. Perrais, C. J. Merrifield, A high precision survey of the molecular dynamics of mammalian Clathrin-Mediated endocytosis. *PLoS Biol.* **9**, e1000604 (2011).

30. A. R. Ramjaun, P. S. McPherson, Multiple amphiphysin II splice variants display differential clathrin binding: Identification of two distinct clathrin-binding sites. *J. Neurochem.* **70**, 2369–2376 (1998).
31. L. Picas *et al.*, BIN1/M-amphiphysin2 induces clustering of phosphoinositides to recruit its downstream partner dynamin. *Nat. Commun.* **5**, 5647 (2014).
32. A. Hohendahl, A. Roux, V. Galli, Structural insights into the centronuclear myopathy-associated functions of BIN1 and dynamin 2. *J. Struct. Biol.* **196**, 37–47 (2016).
33. J. Adam, N. Basnet, N. Mizuno, Structural insights into the cooperative remodeling of membranes by amphiphysin/BIN1. *Sci. Rep.* **5**, 15452 (2015).
34. H. Damke, T. Baba, D. E. Warnock, S. L. Schmid, Induction of mutant dynamin specifically blocks endocytic coated vesicle formation. *J. Cell Biol.* **127**, 915–934 (1994).
35. B. Marks *et al.*, GTPase activity of dynamin and resulting conformation change are essential for endocytosis. *Nature* **410**, 231–235 (2001).
36. R. Ramachandran *et al.*, The dynamin middle domain is critical for tetramerization and higher-order self-assembly. *EMBO J.* **26**, 559–566 (2007).
37. A. Roux *et al.*, Membrane curvature controls dynamin polymerization. *Proc. Natl. Acad. Sci. U.S.A.* **107**, 4141–4146 (2010).
38. S. Dar, T. J. Pucadyil, The pleckstrin-homology domain of dynamin is dispensable for membrane constriction and fission. *Mol. Biol. Cell* **28**, 152–160 (2017).
39. M. Fuhrmans, M. Müller, Coarse-grained simulation of dynamin-mediated fission. *Soft Matter* **11**, 1464–1480 (2015).
40. A. Hohendahl *et al.*, Structural inhibition of dynamin-mediated membrane fission by endophilin. *Elife* **6**, e26856 (2017).
41. K. Takei, V. I. Slepnev, V. Haucke, P. D. Camilli, Functional partnership between amphiphysin and dynamin in clathrin-mediated endocytosis. *Nat. Cell Biol.* **1**, 33–39 (1999).
42. J. I. Garzón, J. Kovacs, R. Abagyan, P. Chacón, ADP_EM: Fast exhaustive multi-resolution docking for high-throughput coverage. *Bioinformatics* **23**, 427–433 (2007).
43. J. R. Lopéz-Blanco, P. Chacón, iMODFIT: Efficient and robust flexible fitting based on vibrational analysis in internal coordinates. *J. Struct. Biol.* **184**, 261–270 (2013).
44. A. A. Baykov, O. A. Evtushenko, S. M. Avaeva, A malachite green procedure for orthophosphate determination and its use in alkaline phosphatase-based enzyme immunoassay. *Anal. Biochem.* **171**, 266–270 (1988).
45. S. C. Kamerkar, F. Kraus, A. J. Sharpe, T. J. Pucadyil, M. T. Ryan, Dynamin-related protein 1 has membrane constricting and severing abilities sufficient for mitochondrial and peroxisomal fission. *Nat. Commun.* **9**, 5239 (2018).
46. J. Schindelin *et al.*, Fiji: An open-source platform for biological-image analysis. *Nat. Methods* **9**, 676–682 (2012).